Photoacoustics 33 (2023) 100562

Contents lists available at ScienceDirect

Photoacoustics

journal homepage: www.elsevier.com/locate/pacs

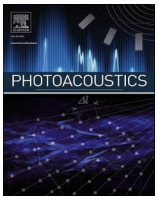

Diagnosis of liver fibrosis and liver function reserve through non-invasive multispectral photoacoustic imaging

Tingting Qiu [a], Jinge Yang [b], Chihan Peng [a], Hongjin Xiang [a], Lin Huang [c], Wenwu Ling [a,*], Yan Luo [a,*]

[a] Department of Ultrasound, West China Hospital, Sichuan University, 37 Guoxue Alley, Wuhou District, Chengdu 610041, China
[b] School of Optoelectric Engineering, Chongqing University of Posts and Telecommunications, Chongqing 400065, China
[c] School of Electronic Science and Engineering, University of Electronic Science and Technology of China, No.2006, Xiyuan Ave, West Hi-Tech Zone District, Chengdu 611731, China

ARTICLE INFO

Keywords:
Liver fibrosis
Liver function
Indocyanine green
Photoacoustic imaging

ABSTRACT

Liver function reserve (LFR) is the sum of remnant functional hepatic cells after liver injury. In the pathologic process of liver fibrosis (LF), LFR is impaired. LFR assessment can help determine the safe scope of liver resection or drug regimen and predict prognosis of patients with liver disease. Here, we used a photoacoustic imaging (PAI) system to assess LF and LFR in rabbit models. We performed PAI, ultrasound elastography and biopsy for 21 rabbits developing none (n = 6) and LF (n = 15). In vivo indocyanine green (ICG) measurements by PAI showed that LF group presented a significantly attenuated ICG clearance compared to control group, indicating LFR impairment of LF. Another finding was a significantly higher collagen photoacoustic signal intensity value was observed in LF both in vivo and in vitro. Our findings demonstrated that PAI was potentially effective to evaluate LFR and collagen accumulation of LF.

1. Introduction

Liver fibrosis is a chronic pathological process characterized by the repeated injury of the liver, as well as the abnormal proliferation and accumulation of fibrous tissue. This progressive scarring is predominantly associated with infections caused by hepatitis B or C, obesity, and prolonged alcohol abuse, which have significant social and economic implications on a global scale [1–3].

The "gold standard" for diagnosis of liver fibrosis is biopsy, which is invasive and expensive, with risk of bleeding and sampling variability. Among non-invasive methods, liver stiffness value (LSV) measured by ultrasound elastography is a relatively reliable marker to reflect the severity of liver fibrosis. However, this technique is an indirect way to assess liver fibrosis stage and can be affected by several factors, of which inflammation and hepatic metabolic function may lead to large measurement variation of LSV [4,5]. Liver function reserve (LFR) is the sum of remnant functional hepatic cells after liver injury. In the pathologic process of liver fibrosis, with repeated liver injury and abnormal proliferation and accumulation of fibrosis tissue, LFR is impaired. LFR assessment is clinically important, because LFR can help determine the safe scope of liver resection or drug regimen and predict prognosis of patients with liver disease [6–8]. Indocyanine green (ICG), a U.S. Food and Drug Administration (FDA)–approved dye, which can be selectively taken up by hepatic cells, eliminated through bile in its original form without any metabolic change in liver or extrahepatic intake. Due to this exclusive hepatic clearance, an ICG clearance test is the standard diagnostic approach to evaluate LFR clinically, with the dynamic change of blood ICG concentration measured by spectrophotometry or pulse dye densitometry (PDD). Clinically, indocyanine green retention rate at 15 min (ICGR15) was incorporated in decision tree for selection of operative procedure in patients with impaired liver functional reserve [6–8]. To be more specific, for example, right hepatectomy can be tolerated if the ICGR-15 is $< 10\%$. For patients with ICGR-15 within the range of 10%− 19%, one-third of the liver parenchyma, which corresponds to left hepatectomy and right paramedian or lateral sectoriectomy, can be resected. When the ICGR-15 value range is 20–29%, approximately one-sixth of the liver parenchyma can be resected. Limited resection is indicated in patients with ICGR-15 values of 30% or more. ICGR15 $>$ 40% is contraindication to liver resection. Spectrophotometry is the gold standard to perform ICG clearance test, however, it's an invasive,

* Corresponding authors.
E-mail addresses: lingwenwubing@163.com (W. Ling), luoyan@scu.edu.cn (Y. Luo).

https://doi.org/10.1016/j.pacs.2023.100562
Received 21 May 2023; Received in revised form 21 September 2023; Accepted 25 September 2023
Available online 26 September 2023

complex and not real-time procedure that demands serial blood sampling [9,10]. PDD is non-invasive, but this method cannot provide any imaging guidance. Additionally, according to previous study results the accuracy of PDD is controversial [11]. In our previous published study, we already compared the PAI method for LFR assessment to the gold standard spectrophotometry and verified its accuracy [12]. Other LFR evaluation modalities are either unreliable such as blood test, or with high cost of time and money and unsuitable for frequent screening such as Technetium-99 m diethylenetriaminepentaacetic acid galactosyl human serum albumin single photon emission computed tomography (99mTc-GSA SPECT) and gadoxetic acid-enhanced magnetic resonance imaging (MRI) [13,14].

Based on optical absorption, photoacoustic imaging (PAI) provides structural and functional information with high resolution [15]. It's a non-invasive, fast-developing technique, which has been utilized for in vivo imaging from organelles to organs such as breast [16], thyroid[17], skin [18], bowel [19], prostate [20] and musculoskeletal system [21]. PAI studies on liver evaluated hepatic fat rate or fibrosis severity by photoacoustic spectral analysis in mice, which showed significantly increased PA features in fibrotic or fatty livers versus healthy livers [22,23]. However, these studies did not investigate LFR change during the pathologic process of liver. Based on the unique optical absorption properties of endogenous or exogeneous chromophores, PAI has the ability to quantify hemoglobin, melanin, lipids, collagen [15,24–26]. ICG is not only a drug for LFR reflection, but also a common exogeneous contrast agent for PAI due to its unique optical absorption spectrum [27–29]. Our previous feasibility study using tissue-mimicking phantoms, in vivo normal and partial hepatectomy rabbit models showed that ICG clearance test can be performed in the way of PAI method [12].

In this study, we further build up liver fibrosis rabbit models. PAI was applied to assess the fibrosis severity and LFR condition in these models. The study result may validate the utility of PAI for liver fibrosis and LFR assessment.

2. Methods

2.1. Photoacoustic tomography system

The PAT system is presented in Fig. 1. For more detail about this system can be found in previous study [12]. The PA imaging set up is based on a Q-switched Nd:YAG-pumped optical parameter oscillator system (Surelite, Continuum, California), a 128-element concave ultrasound transducer array (Japan Probe Corporation, Yokohama, Japan), and a 64-channel DAQ system(NI). The oscillator system is capable of supporting pulses at wavelength from 700 to 960 nm with 4 ns pulse duration at a repetition rate up to 20 Hz. An optic fiber bundle with line shaped illumination profile (40 mm × 10 mm) was set besides the transducer to supply lighting. The incident fluence at 805 nm was within the safety limit of the American National Standards Institute regulations [30]. The concave transducer utilized in our study has a center frequency of approximately 5 MHz with a relative bandwidth of 90%. It features a diameter of 100 mm and is composed of two quarter arc-shaped parts, with each part housing 64 elements. The pitch size of each element is 2 mm wide and 15 mm long. For cross-sectional imaging, the transducer achieves a spatial resolution of ~150 μm. The probe was enclosed with a resin shell covered by a polydimethylsiloxane (PDMS) film (100 μm thickness), and deionized water was filled into the space between the membrane and transducer.

Detected PA signals were amplified through a custom-built pre-amplifier then transferred to a 64-channel analog-to-digital system (8 PXIe5105 cards, National Instrument, Texas, USA) after 2:1 multiplexing with 12-bit digital resolution and 50 MS/s sampling rate. The acquired signals were saved in the onboard computer (PXIe8840, National Instrument, Texas, USA) which also worked as control panels for the PAI system.

2.2. Animal models

The use of experimental animals was approved by the animal ethics committee of West China Hospital, Sichuan University. New Zealand rabbits (n = 24, male, weight: 2.5–2.7 kg) were fed with food and water for a week of acclimatization period and then were randomly assigned into liver fibrosis (LF) group (n = 18) and control group (n = 6). For LF group, liver fibrosis was induced by subcutaneous injection of 0.3 ml/kg 50% carbon tetrachloride (CCl_4, Beijing Chemical Reagent Company, Beijing, China) in olive oil as a vehicle, twice a week. For control group, rabbits received subcutaneous injection of 0.3 ml/kg olive oil, twice a week. After 24 weeks, rabbits from both groups undertook procedures of ultrasound elastography, PAI imaging of liver and liver biopsy. Rabbits that died before these procedures were excluded.

2.3. Ultrasound elastography examination

All ultrasound real-time shear wave elastography (SWE) examinations were performed with a standard SWE, Resona 7 ultrasound system (Mindray Medical International, Shenzhen, China) equipped with L9–3 U (linear 3–9 MHz) transducer. The rabbit was anesthetized by isoflurane gas inhalation in the lab at a room temperature of 26 centigrade. After anesthesia, the rabbit was placed in supine position and the fourth right rib to the abdomen was exposed for liver ultrasound scanning by shaving the hair. The L9–3 U probe was gently moved without exerting any pressure. The left lateral liver lobe was displayed on grey-scale ultrasound through subxiphoid section. With the probe maintained in the same place and the left lateral lobe steadily displayed, the sound touch elastography mode was switched on. A color-coded 2D quantitative SWE image was displayed in box form over a conventional B-mode image. A round region of interest (ROI) was placed in the box. Liver stiffness value (LSV) was measured at least 1 cm below the liver capsule in the left lateral lobe. The mean LSV of five consecutive measurements was used for statistical analyses. The image quality is controlled:

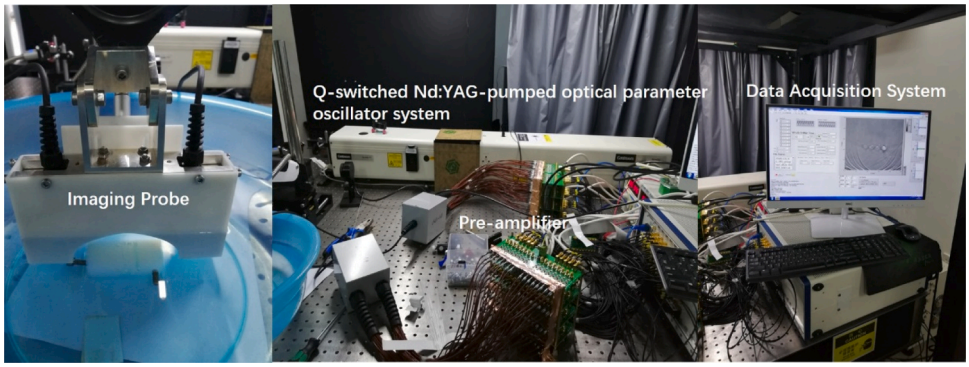

Fig. 1. The set up of photoacoustic tomography system.

homogeneous color filling of the color box > 90% and reliable (RLB) index > 90%. Homogenous color filling of the box means the acquisition box to measure stiffness was filled with color, with color defects area< 10%. The color stands for stiffness values that are quantitatively expressed as Young's modulus in kilopascals (kPa). The Resona 7 system also offers reliability (RLB) indicators of motion stability (M-STB) index and RLB map. Liver stiffness measurements were considered valid when both the M-STB index displayed at least four stars and the RLB map was uniform green, with an index > 90% [31–33].

2.4. In vivo liver PAI

Rabbits from LF and control group were anesthetized by isoflurane gas inhalation in the lab at a room temperature of 26 centigrade. The rabbit was in supine position. The anatomical regions of interest were scanned using a commercial ultrasound platform (iNSIGHT 23 R, Saset Healthcare, Inc. Chengdu, China) with 7.5 MHz line transducer array by a single professional operator. The same left lateral liver lobe demonstrated during elastography examination was displayed on grey-scale ultrasound through subxiphoid section. The location of B-mode ultrasound probe was marked. Then photoacoustic image was obtained by placing the photoacoustic probe in the same position as the B-mode ultrasound probe. Animal posture and the position of the probe (ultrasonic and photoacoustic) were standardized to ensure the repeatability of scanning.

For in vivo imaging, multispectral PA signals were acquired at 730, 760, 800, 850, 900, 920, 930, 950 nm to obtain oxygenated hemoglobin (HbO_2), deoxygenated hemoglobin (HbR), lipid and collagen according to previous studies [34]. To remove the breathing-related artifact, we built a MATLAB code as described previously [35,36]. We calculate the correlation coefficient among all 20 frames from single wavelength and generate a 2D matrix with 20 rows and 20 columns. Using the k-means method, we cluster the frames into two sets based on their correlation coefficients: one set with high correlation coefficients and another with low correlation coefficients. Frames with low correlation coefficients, usually below 0.7, which are affected by motion, are subsequently discarded. The selected frames are then averaged. On average, 12–14 images were retained based on the anesthesia condition (Fig. 2).

2.5. In vivo ICG concentration measurement by PAT

After in vivo liver PAI, the rabbit was in right or left lateral position. Before the PAT scan, ICG was dissolved in distilled water to obtain a concentration of 5 mg/ml. One ear was shaved and fixed on a flat plate with central auricular artery (CAA) clearly visible. Transverse PAT sections of CAA was displayed as the region of interest (ROI) in Fig. 2. PAT scan was performed over CAA at 805 nm for 20 min at an acquisition rate of 1 frame per second (Time-averaged for 10 consecutive frames). After 1 min of PAT baseline scan, a dose of 0.1 ml/kg ICG solution was injected via the left auricular vein along with 5 ml saline flush for 10 s, simultaneously PAT signal was continuously acquired for additional 19 min. Based on the exclusive hepatic clearance and first-order kinetics of ICG, ICG concentration change in the blood reflects the hepatic ability of ICG clearance. Therefore, it's reasonable to monitor ICG concentration change in the blood through any peripheral vasculature. The reason that we scanned auricular artery by PAI because it's a very superficial structure for PAI scanning. Still based on the pharmacokinetics of ICG, ICG can reach its peak rapidly after entering the body no matter what vasculature you choose to inject ICG. Clinically, ICG was injected through median cubital vein in human. We chose auricular vein in the rabbit to make the injection because it's easier to operate compared to other sites.

2.6. In vitro liver tissue PAI

After in vivo experiment, representative tissue specimens were taken from previously imaged anatomical regions. After harvesting, tissue specimens from the same lobe were divided into two parts, one for ex vivo PA imaging, and the other one was fixed in a 4% formaldehyde/PBS solution and then embedded in paraffin. For the ex vivo PA imaging, multispectral PA signals were acquired at 730, 760, 800, 850, 900, 920, 930, 950 nm (Fig. 3).

2.7. Image reconstruction and analysis

PA data collected were first reconstructed in Labview (NI, USA) using back-projection algorithm in real-time [37]. The raw PA data were also stored for offline processing by Matlab (R2016b, Mathworks, Inc., MA, USA). In the offline processing, 0.2–10 MHz filtering was applied to remove high frequency noise, and then PA images were reconstructed offline using back-projection schemes [38].

A linear un-mixing was applied to obtain the signal from four endogenous absorbers (HbO_2 , HbR , lipid, collagen) following previous studies [23,38]. Collagen unmixing was based on all wavelengths

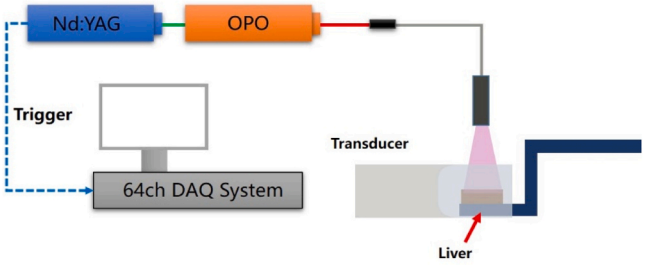

Fig. 3. The hardware components employed in *ex vivo* experiments. **DAQ**: Data Acquisition System (preamplifiers, multiplexers and analog-to-digital converters). **OPO**: Optical parameter oscillator system. **PC**: personal computer. **Nd:YAG**: Nd:YAG bumping laser.

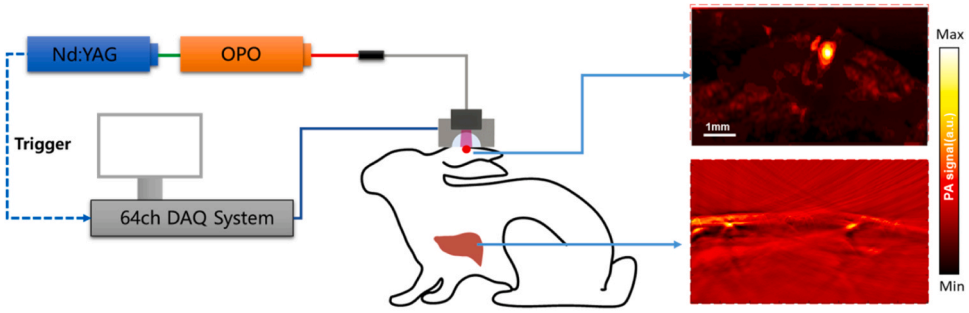

Fig. 2. A schematic of the in vivo PAI experimental system. **DAQ**: Data Acquisition System (preamplifiers, multiplexers and analog-to-digital converters)。 **Nd:YAG**: Nd:YAG bumping laser. **OPO**: Optical parameter oscillator system. **PC**: Personal computer. **Imaging Probe**: a 128-element transducer array, a fiber bundle, and a resin shell enclosed with a membrane.

(730, 760, 800, 850, 900, 920, 930 and 950 nm), whereas the HbR and HbO_2 signals were calculated from a sub-range (760, 800 and 850 nm), which is more accurate in unmixing due to increased water absorptivity at higher wavelength [21]. The total hemoglobin (HbT = HbR+HbO_2), lipid and collagen values were calculated from 2 mm × 5 mm regions of interest close to the surface of the skin to minimize error due to the linear unmixing [21,23,39]. The averaged HbT signal, (HbT_{mean}), lipid signal ($lipid_{mean}$) and collagen signal ($collagen_{mean}$) were calculated for statistical analysis.

2.8. Pathologic examination

After imaging examination, liver tissue specimens were obtained, fixed with 10% formalin and embedded in paraffin. Liver tissue sections were stained with haematoxylin–eosin (H&E) and Masson's trichrome stains. Liver fibrosis was staged according to the METAVIR scoring system as follows: F0, no fibrosis; F1, enlarged fiber proliferation on portal tracts; F2, peripheral fibrosis in the portal area with few fiber septa formation and intact architecture of the liver lobule; F3, fibrous septum accompanied by intralobular structural disorders but without cirrhosis; F4, cirrhosis. The degree of inflammation and necrosis was graded on a scale of 0–4 (0 =absent, 1 =slight, 2 =mild, 3 =moderate, 4 =severe).

2.9. Statistical analysis

Statistical analysis and graphical display of data were performed using GraphPad software (version 7.00; GraphPad Software, San Diego, CA, USA). In the ICG results, continuous variables were given as means and standard deviation (SD) in the manually selected ROI region at the CAA. Averaged PA signal in the CAA were normalized as the relative photoacoustic signal intensity (PSI_{re}) to reflect the ICG concentration change as follows:

$$PSI_{re}(t) = \frac{PSI(t) - PSI_{base}}{PSI_{base}}$$

PSI_{base} is the base PSI before ICG injection which generated from hemoglobin. $PSI(t)$ is the PSI at time t. To quantify the kinetics of PSI_{re} change after the ICG injection, an exponential decay model [40] was used as follows:

$$PSI_{re}(t) = PSI_{re}(0)e^{-kt}$$

where the elimination time (t_0) indicates the elapse time from $PSI_{re}(0)$to the baseline. The rate constant (k) gives the decay rate.

Multi-wavelength photoacoustic signals were obtained from 20 frames of rabbit liver. Frames moving due to breathing are excluded by the custom breathing program in Matlab. Matlab was used to register the remaining images and take the mean value for spectral separation. A mean total hemoglobin (HbT_{mean}), lipid signal ($lipid_{mean}$) and collagen signal ($collagen_{mean}$) were calculated over regions of interest of liver. According to METAVIR scoring system, *In vivo* and *ex vivo* statistical analysis between two groups (fibrosis versus control) of PA parameters and liver stiffness values were conducted using independent samples t-tests. For comparison of PA parameters and liver stiffness values among different stages of liver fibrosis, ANOVA and Tukey's multiple comparison test or Welch test and DunnettT3 multiple comparison test was applied. Pearson correlation test was used to investigate the correlation between in vivo and ex vivo collagen signal and their correlation with liver stiffness values respectively. A value of $p < 0.05$ was considered statistically significant.

3. Results

3.1. Liver fibrosis models

Three rabbits died of acute liver failure in 0.5–2 days after percutaneous injection of 50% CCl4 in the LF group. Finally, 15 rabbits in the LF group and 6 rabbits in the control group were enrolled for statistical analysis. Through Masson dye (Fig. 4, first column) of liver tissue, LF group displayed the increased accumulation of collagen fibers (blue region) over fibrosis stages and no fibrosis was presented in the control group. Mean fiber expression percentage by Masson dye was displayed in Table 1.

By H&E dye (Fig. 4, second column) of liver tissue, different degrees of hepatic cell necrosis and inflammatory cell infiltration were observed in LF group. Shear wave elastography (Fig. 4, third column) measurements showed increased liver stiffness values of different fibrosis stages. The last three columns were PA images of hemoglobin (Fig. 4, fourth column), lipid (Fig. 4, fifth column), and collagen (Fig. 4, sixth column) of different fibrosis stages. According to METAVIR scoring system, F0, no fibrosis (n = 6); F1, enlarged fiber proliferation on portal tracts (n = 3); F2, peripheral fibrosis in the portal area with few fiber septa formation and intact architecture of the liver lobule (n = 5); F3, fibrous septum accompanied by intralobular structural disorders but without cirrhosis (n = 4); F4, cirrhosis (n = 3).

3.2. Liver stiffness values measurement in vivo

Liver stiffness value (median, range) was displayed in Table 2. With liver fibrosis development, LSV gradually increased, LSV of control group was significantly lower than that of liver fibrosis group (10.16kPa vs. 22.57kPa, $p < 0.0001$). Multiple comparison of LSV between F0-F4 showed that LSV between adjacent fibrosis stage was not significantly different, but LSV between F0 vs. F2 ($p = 0.0071$), F0 vs. F3 ($p = 0.0024$), F0 vs. F4($p < 0.0001$), F1 vs. F3($p = 0.0499$), F1 vs. F4 ($p = 0.0006$), F2 vs. F4 ($p = 0.0240$) was significantly different.

3.3. ICG clearance test in vivo

As illustrated in Fig. 5a, in vivo ICG measurement result showed that after injection of ICG at 60 s time point, a high-intensity peak was observed and gradually decreased over time. Statistical results for rate constant k displayed high value in the control group (k_1 vs. k_2, 0.01858 ± 0.0027 vs. 0.00595 ± 0.0045, $p < 0.0001$), while lower value in the liver fibrosis group. The time to recovery t_0 showed significant differences between the two groups (t_{01} vs. t_{02}, 199.8 ± 40.57 s vs. 549.6 ± 203.5 s, $p = 0.0007$) (Fig. 5b).

3.4. In vivo and in vitro: collagen, lipid, HbT

Table 3 and Fig. 6 displayed in vivo and in vitro PAI study results. In vivo study result presented that a significantly higher collagen PSI value was observed in fibrosis group ($p = 0.0017$). A significantly higher lipid PSI value was observed in fibrosis group ($p < 0.0001$). Total hemoglobin (HbT) PSI value was similar between control and fibrosis group ($p = 0.764$). In vitro study result showed that a significantly higher collagen PSI value was observed in fibrosis group ($p = 0.0009$). A significantly higher lipid PSI value was observed in fibrosis group ($p < 0.0001$). A significantly higher total hemoglobin (HbT) PSI value was observed in control group ($p = 0.0013$).

3.5. Correlation between collagen PSI and LSV, collagen PSI and Mean fiber expression percentage in vivo vs. in vitro

In vivo study, collagen PSI was strongly correlated with LSV (Pearson $r = 0.8413$, $p < 0.0001$), collagen PSI was highly correlated with mean fiber expression percentage (Pearson $r = 0.7717$, $p < 0.0001$).

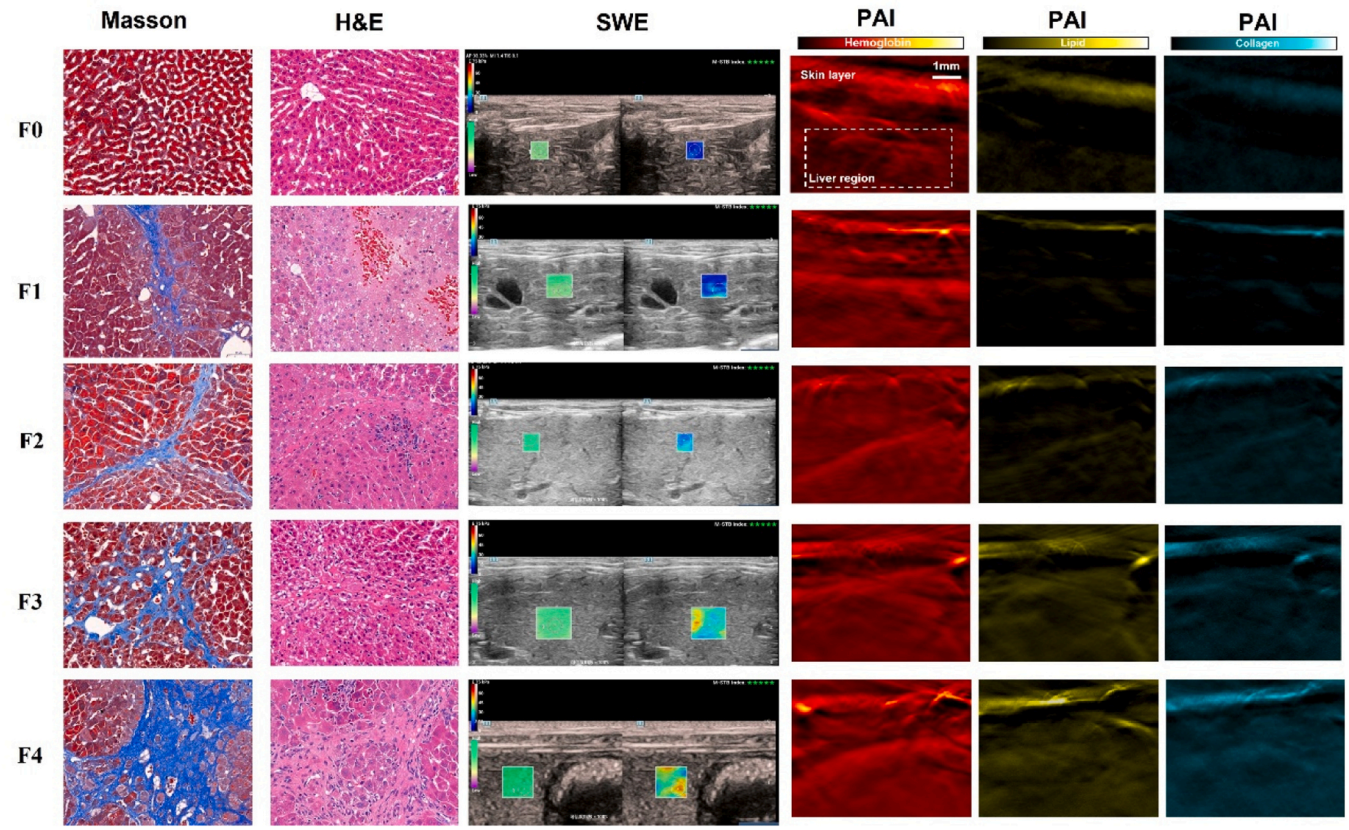

Fig. 4. First column, MASSON dye. Second column, H&E dye. Third column, liver stiffness value measurement by SWE. Fourth column, PAI of Hb. Fifth column, PAI of lipid. Sixth column, PAI of collagen.

Table 1
Mean fiber expression percentage of different liver fibrosis stage.

Liver fibrosis stage	Mean fiber expression percentage	SD
F0	0.233	0.221
Fibrosis	19.30	11.90
F1	5.060	0.813
F2	14.03	6.109
F3	23.30	5.095
F4	36.97	1.594

SD, standard deviation

Table 2
Liver stiffness value of different liver fibrosis stage.

Liver fibrosis stage	LSV (median, kPa)	LSV (range, kPa)
F0	10.16	8.48–12.09
Fibrosis	22.57	12.0–42.03
F1	13.26	12.0–15.49
F2	22.39	13.64–31.56
F3	24.02	21.65–32.42
F4	33.18	31.96–42.03

In vitro study, collagen PSI was positively correlated with LSV (Pearson $r = 0.6525$, $p = 0.0013$), collagen PSI was strongly correlated with mean fiber expression percentage (Pearson $r = 0.8602$, $p < 0.0001$)..

4. Discussion

Liver fibrosis is a type of "silent" chronic pathological change: repeated liver injury with fibers dysplasia and deposition. This progressive scarring of the liver in humans is often caused by hepatitis B, hepatitis C virus, obesity, or chronic alcohol abuse, and imposes a huge social and economic burden [41,42]. In this study, liver fibrosis model was induced by low dose of CCl_4, the mechanism of which is to cause liver cell necrosis, thus stimulating fibrous hyperplasia and gradually forming liver fibrosis and cirrhosis. Then liver stiffness values (LSVs) of these fibrosis models were measured by SWE. The results showed that with fibrosis progression, LSVs of fibrosis group increased and were significantly higher than those of control group, which were consistent with pathologic change of liver fibrosis and previous related reports [33,43,44].

In the process of liver fibrosis, necrosis of liver cells and proliferation of fibrous tissue leads to LFR impairment theoretically. In this study, LFR of New Zealand rabbits was evaluated by PAI combined with ICG via central auricular artery. The results demonstrated that the clearance rate of ICG in the control group was significantly higher than that in the liver fibrosis group, and the clearance time in the control group was significantly shorter than that in the liver fibrosis group, which indicated the damage of LFR in the process of liver fibrosis. Previous study reported that in the process of liver fibrosis in human or animal, ICGR15 (generally ICGR15 >10% indicating LFR damage) were significantly elevated, which supported our study results to some degree. However, different from the PAI method for LFR assessment in this study, most published studies applied spectrophotometric analysis or PDD for ICGR15 measurement, which is either invasive and complicated or the accuracy is controversial [9–11]. In this study, PAI combined with ICG was used to monitor LFR in real time. In our previous work, strong correlation between PAI and spectrophotometry was observed, which confirmed the accuracy of PAI method for LFR assessment [12]. Therefore, it can be concluded that PAI combined with ICG can effectively reflect the damage of LFR in a living New Zealand rabbit model of liver fibrosis.

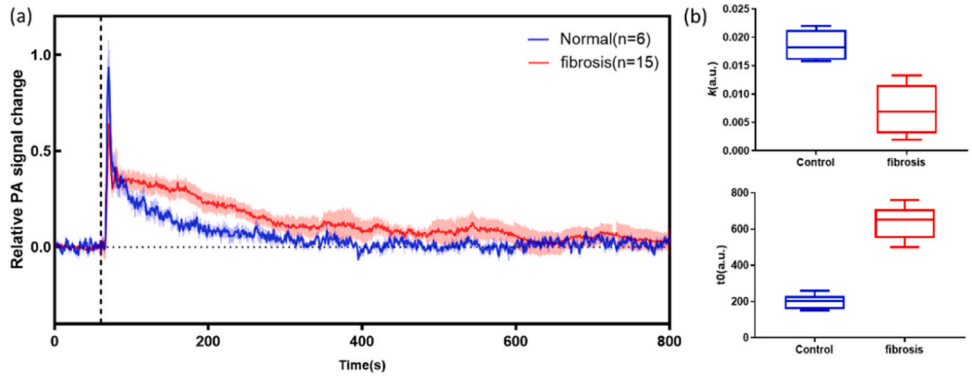

Fig. 5. ICG clearance studies between fibrosis and control groups of rabbits (fibrosis, n = 15, control group, n = 6). (a). Temporal PA signal trace from 21 rabbits in two groups. For each curve, data were normalized to the highest intensity acquired. (b) Elimination rate constant k (top) and elimination time t0 (bottom).

Table 3
$Collagen_{mean}$, $Lipid_{mean}$, HbT in vivo vs. in vitro.

	Control (F0)	Fibrosis	F1	F2	F3	F4
In vivo						
Collagen	0.028 ± 0.021	0.109 ± 0.052	0.055 ± 0.008	0.081 ± 0.041	0.151 ± 0.040	0.156 ± 0.005
Lipid	0.044 ± 0.023	0.262 ± 0.117	0.155 ± 0.054	0.200 ± 0.078	0.306 ± 0.047	0.415 ± 0.105
HbT	0.893 ± 0.082	0.733 ± 0.199	0.647 ± 0.176	0.840 ± 0.213	0.682 ± 0.275	0.683 ± 0.070
In vitro						
Collagen	0.053 ± 0.027	0.126 ± 0.041	0.111 ± 0.008	0.094 ± 0.026	0.135 ± 0.042	0.180 ± 0.025
Lipid	0.056 ± 0.024	0.280 ± 0.119	0.146 ± 0.045	0.224 ± 0.060	0.325 ± 0.057	0.445 ± 0.071
HbT	2.015 ± 0.252	1.480 ± 0.308	1.241 ± 0.155	1.412 ± 0.371	1.784 ± 0.175	1.429 ± 0.178

ICG clearance test, as an index to evaluate LFR of rabbits with liver fibrosis, showed that LFR got injured in the process of liver fibrosis. But this method can't quantify the degree of liver fibrosis. Compared with existing imaging modalities, including ultrasound and MRI, multispectral PAI is a target-specific, quantitative and non-invasive imaging modality. In order to obtain more specific liver fibrosis information, we performed multispectral PAI in vivo and in vitro. Liver fibrosis group presented significantly increased hepatic collagen fiber content than the control group, which was in good agreement with ultrasound elastography and pathological results, indicating the abnormal accumulation of collagen fibers in the liver [45,46]. In addition, in vitro and in vivo PAI results showed that lipid components gradually increased with the progression of liver fibrosis, suggesting abnormal lipid metabolism in liver during fibrosis pathology. In general, multispectral PAT can detect abnormal deposition of collagen fibers during liver fibrosis, which is consistent with similar results obtained recently in mice [23].

Limitations of this study. First, the sample size of different stages of liver fibrosis in this study is small, and further expansion of sample size is needed to improve the test power. Second, clinically, various etiologies such as virus (HBV, HCV), alcohol, drugs or toxicants can cause liver damage. The basic pathogenic mechanism of these various etiologies is to cause hepatic cell degeneration or necrosis, stimulate fibrous tissue hyperplasia. CCl4 damage to the liver conforms to the basic pathogenic mechanism, but it's not the same liver damage as that in a clinical scene. Oil red O for lipid presentation in the pathologic results was not performed. PA imaging of lipid in fibrosis animal model in this study is a preliminary try, however it lacks accurate quantitative pathologic evidence. Third, one ultrasound system with elastography mode should be used to locate liver lobe and measure liver stiffness. Fourth, linear un-mixing analysis. Advanced spectral un-mixing methods need to be developed to achieve the capability of refined quantification of PA signal.

5. Conclusion

Photoacoustic tomography was potentially useful to reflect LFR impairment and collagen accumulation in liver fibrosis models of New Zealand rabbits.

Declaration of Competing Interest

The authors declare that they have no known competing financial interests or personal relationships that could have appeared to influence the work reported in this paper.

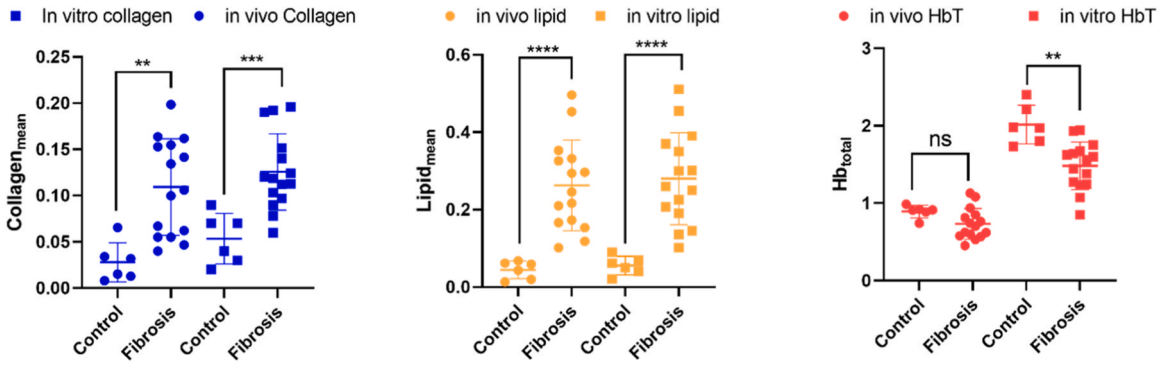

Fig. 6. $Collagen_{mean}$, $Lipid_{mean}$, HbT for control and fibrosis rabbits. Each circle and cube represents the mean PA signal per independent liver region in vivo and in vitro respectively.

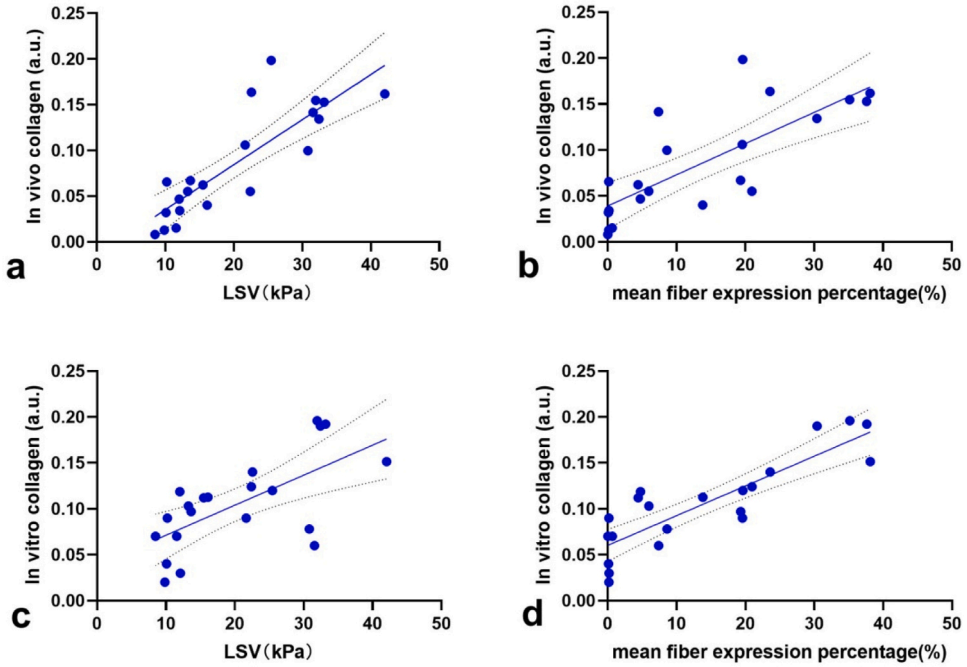

Fig. 7. Correlations between in vivo collagen vs. LSV, in vivo collagen vs. mean fiber expression percentage, in vitro collagen vs. LSV, in vitro collagen vs. mean fiber expression percentage LSV=liver stiffness value.

Data Availability

The data that has been used is confidential.

Acknowledgments

This work was supported by the National Natural Science Foundation of China (82001833). We thank Professor. Zhe Wu from University of Electronic Science and Technology of China and Huabei Jiang from University of South Florida for professional advice in the preparation of the article.

References

[1] European Association for the Study of the Liver, . Electronic address: easloffice@easloffice.eu, European Association for the Study of the Liver, EASL Clinical Practice Guidelines for the management of patients with decompensated cirrhosis, J. Hepatol. 69 (2018) 406–460, https://doi.org/10.1016/j.jhep.2018.03.024.

[2] Y.-F. Liaw, J.-H. Kao, T. Piratvisuth, H.L.Y. Chan, R.-N. Chien, C.-J. Liu, E. Gane, S. Locarnini, S.-G. Lim, K.-H. Han, D. Amarapurkar, G. Cooksley, W. Jafri, R. Mohamed, J.-L. Hou, W.-L. Chuang, L.A. Lesmana, J.D. Sollano, D.-J. Suh, M. Omata, Asian-Pacific consensus statement on the management of chronic hepatitis B: a 2012 update, Hepatol. Int. 6 (2012) 531–561, https://doi.org/10.1007/s12072-012-9365-4.

[3] F.-S. Wang, J.-G. Fan, Z. Zhang, B. Gao, H.-Y. Wang, The global burden of liver disease: the major impact of China, Hepatology 60 (2014) 2099–2108, https://doi.org/10.1002/hep.27406.

[4] R.G. Barr, G. Ferraioli, M.L. Palmeri, Z.D. Goodman, G. Garcia-Tsao, J. Rubin, B. Garra, R.P. Myers, S.R. Wilson, D. Rubens, D. Levine, Elastography assessment of liver fibrosis: society of radiologists in ultrasound consensus conference statement, Radiology 276 (2015) 845–861, https://doi.org/10.1148/radiol.2015150619.

[5] E.B. Tapper, E.B. Cohen, K. Patel, B. Bacon, S. Gordon, E. Lawitz, D. Nelson, I. A. Nasser, T. Challies, N. Afdhal, Levels of alanine aminotransferase confound use of transient elastography to diagnose fibrosis in patients with chronic hepatitis C virus infection, Clin. Gastroenterol. Hepatol. 10 (2012) 932–937, https://doi.org/10.1016/j.cgh.2012.01.015, e1.

[6] L.T. Hoekstra, W. de Graaf, G.A.A. Nibourg, M. Heger, R.J. Bennink, B. Stieger, T. M. van Gulik, Physiological and biochemical basis of clinical liver function tests: a review, Ann. Surg. 257 (2013) 27–36, https://doi.org/10.1097/SLA.0b013e31825d5d47.

[7] H. Imamura, K. Sano, Y. Sugawara, N. Kokudo, M. Makuuchi, Assessment of hepatic reserve for indication of hepatic resection: Decision tree incorporating indocyanine green test, J. Hepatobiliary Pancreat. Surg. 12 (2005) 16–22, https://doi.org/10.1007/s00534-004-0965-9.

[8] F. Manizate, S.P. Hiotis, D. Labow, S. Roayaie, M. Schwartz, Liver functional reserve estimation: state of the art and relevance to local treatments, Oncology 78 (Suppl 1) (2010) 131–134, https://doi.org/10.1159/000315241.

[9] P. Ott, Hepatic elimination of indocyanine green with special reference to distribution kinetics and the influence of plasma protein binding, Pharm. Toxicol. (1998), https://doi.org/10.1111/j.1600-0773.1998.tb01945.x.

[10] C.K. Svensson, D.J. Edwards, D. Lalka, P.M. Mauriello, E. Middleton, Comparison of chromatographic and spectrophotometric analysis of indocyanine green in plasma following administration of multiple doses to humans, J. Pharm. Sci. (1982), https://doi.org/10.1002/jps.2600711134.

[11] T. Imai, K. Takahashi, F. Goto, Y. Morishita, Measurement of blood concentration of indocyanine green by pulse dye densitometry–comparison with the conventional spectrophotometric method, J. Clin. Monit. Comput. 14 (1998) 477–484, https://doi.org/10.1023/a:1009948128543.

[12] T. Qiu, J. Yang, T. Pan, C. Peng, H. Jiang, Y. Luo, Assessment of liver function reserve by photoacoustic tomography: a feasibility study, Biomed. Opt. Express 11 (2020) 3985–3995, https://doi.org/10.1364/BOE.394344.

[13] M. Nakagawa, T. Namimoto, K. Shimizu, K. Morita, F. Sakamoto, S. Oda, T. Nakaura, D. Utsunomiya, S. Shiraishi, Y. Yamashita, Measuring hepatic functional reserve using T1 mapping of Gd-EOB-DTPA enhanced 3T MR imaging: a preliminary study comparing with 99mTc GSA scintigraphy and signal intensity based parameters, Eur. J. Radio. 92 (2017) 116–123, https://doi.org/10.1016/j.ejrad.2017.05.011.

[14] A. Kato, Y. Nakamoto, T. Ishimori, S. Seo, S. Uemoto, K. Togashi, Predictability of 99mTc-Galactosyl human serum albumin scintigraphy for posthepatectomy liver failure, AJR Am. J. Roentgenol. 210 (2018) 158–165, https://doi.org/10.2214/AJR.17.18411.

[15] L.V. Wang, S. Hu, Photoacoustic tomography: In vivo imaging from organelles to organs, Science (1979) (2012), https://doi.org/10.1126/science.1216210.

[16] X.L. Deán-Ben, T.F. Fehm, M. Gostic, D. Razansky, Volumetric hand-held optoacoustic angiography as a tool for real-time screening of dense breast, J. Biophotonics 9 (2016) 253–259, https://doi.org/10.1002/jbio.201500008.

[17] M. Yang, L. Zhao, X. He, N. Su, C. Zhao, H. Tang, T. Hong, W. Li, F. Yang, L. Lin, B. Zhang, R. Zhang, Y. Jiang, C. Li, Photoacoustic/ultrasound dual imaging of human thyroid cancers: an initial clinical study, Biomed. Opt. Express 8 (2017) 3449, https://doi.org/10.1364/boe.8.003449.

[18] I. Steinberg, D.M. Huland, O. Vermesh, H.E. Frostig, W.S. Tummers, S.S. Gambhir, Photoacoustic clinical imaging, Photoacoustics 14 (2019) 77–98, https://doi.org/10.1016/j.pacs.2019.05.001.

[19] F. Knieling, C. Neufert, A. Hartmann, J. Claussen, A. Urich, C. Egger, M. Vetter, S. Fischer, L. Pfeifer, A. Hagel, C. Kielisch, R.S. Görtz, D. Wildner, M. Engel, J. Röther, W. Uter, J. Siebler, R. Atreya, W. Rascher, D. Strobel, M.F. Neurath, M. J. Waldner, Multispectral optoacoustic tomography for assessment of Crohn's disease activity, N. Engl. J. Med. 376 (2017) 1292–1294, https://doi.org/10.1056/NEJMc1612455.

[20] S.-R. Kothapalli, G.A. Sonn, J.W. Choe, A. Nikoozadeh, A. Bhuyan, K.K. Park, P. Cristman, R. Fan, A. Moini, B.C. Lee, J. Wu, T.E. Carver, D. Trivedi, L. Shiiba, I. Steinberg, D.M. Huland, M.F. Rasmussen, J.C. Liao, J.D. Brooks, P.T. Khuri-Yakub, S.S. Gambhir, Simultaneous transrectal ultrasound and photoacoustic

human prostate imaging, Sci. Transl. Med. 11 (2019), https://doi.org/10.1126/scitranslmed.aav2169.
[21] A.P. Regensburger, L.M. Fonteyne, J. Jüngert, A.L. Wagner, T. Gerhalter, A. M. Nagel, R. Heiss, F. Flenkenthaler, M. Qurashi, M.F. Neurath, N. Klymiuk, E. Kemter, T. Fröhlich, M. Uder, J. Woelfle, W. Rascher, R. Trollmann, E. Wolf, M. J. Waldner, F. Knieling, Detection of collagens by multispectral optoacoustic tomography as an imaging biomarker for Duchenne muscular dystrophy, Nat. Med. 25 (2019) 1905–1915, https://doi.org/10.1038/s41591-019-0669-y.
[22] G. Xu, Z.-X. Meng, J.D. Lin, J. Yuan, P.L. Carson, B. Joshi, X. Wang, The functional pitch of an organ: quantification of tissue texture with photoacoustic spectrum analysis, Radiology 271 (2014) 248–254, https://doi.org/10.1148/radiol.13130777.
[23] P.J. van den Berg, R. Bansal, K. Daoudi, W. Steenbergen, J. Prakash, Preclinical detection of liver fibrosis using dual-modality photoacoustic/ultrasound system, Biomed. Opt. Express 7 (2016) 5081–5091, https://doi.org/10.1364/BOE.7.005081.
[24] X. Shu, H. Li, B. Dong, C. Sun, H.F. Zhang, Quantifying melanin concentration in retinal pigment epithelium using broadband photoacoustic microscopy, Biomed. Opt. Express 8 (2017) 2851–2865, https://doi.org/10.1364/BOE.8.002851.
[25] G.S. Sangha, E.H. Phillips, C.J. Goergen, In vivo photoacoustic lipid imaging in mice using the second near-infrared window, Biomed. Opt. Express 8 (2017) 736, https://doi.org/10.1364/BOE.8.000736.
[26] Y. Yan, N. Gomez-Lopez, M. Basij, A.V. Shahvari, F. Vadillo-Ortega, E. Hernandez-Andrade, S.S. Hassan, R. Romero, M. MehrMohammadi, Photoacoustic imaging of the uterine cervix to assess collagen and water content changes in murine pregnancy, Biomed. Opt. Express 10 (2019) 4643–4655, https://doi.org/10.1364/BOE.10.004643.
[27] S. Park, J. Kim, M. Jeon, J. Song, C. Kim, In vivo photoacoustic and fluorescence cystography using clinically relevant dual modal indocyanine green, Sensors 14 (2014) 19660–19668, https://doi.org/10.3390/s141019660.
[28] J. Lavaud, M. Henry, P. Gayet, A. Fertin, J. Vollaire, Y. Usson, J.-L. Coll, V. Josserand, Noninvasive monitoring of liver metastasis development via combined multispectral photoacoustic imaging and fluorescence diffuse optical tomography, Int J. Biol. Sci. 16 (2020) 1616–1628, https://doi.org/10.7150/ijbs.40896.
[29] M.D. Mokrousov, M.V. Novoselova, J. Nolan, W. Harrington, P. Rudakovskaya, D. N. Bratashov, E.I. Galanzha, J.P. Fuenzalida-Werner, B.P. Yakimov, G. Nazarikov, V.P. Drachev, E.A. Shirshin, V. Ntziachristos, A.C. Stiel, V.P. Zharov, D.A. Gorin, Amplification of photoacoustic effect in bimodal polymer particles by self-quenching of indocyanine green, Biomed. Opt. Express 10 (2019) 4775, https://doi.org/10.1364/BOE.10.004775.
[30] E. Mercep, X.L. Dean-Ben, D. Razansky, Combined Pulse-Echo ultrasound and multispectral optoacoustic tomography with a multi-segment detector array, IEEE Trans. Med Imaging (2017), https://doi.org/10.1109/TMI.2017.2706200.
[31] T. Shiina, K.R. Nightingale, M.L. Palmeri, T.J. Hall, J.C. Bamber, R.G. Barr, L. Castera, B.I. Choi, Y.-H. Chou, D. Cosgrove, C.F. Dietrich, H. Ding, D. Amy, A. Farrokh, G. Ferraioli, C. Filice, M. Friedrich-Rust, K. Nakashima, F. Schafer, I. Sporea, S. Suzuki, S. Wilson, M. Kudo, WFUMB guidelines and recommendations for clinical use of ultrasound elastography: Part 1: basic principles and terminology, Ultrasound Med Biol. 41 (2015) 1126–1147, https://doi.org/10.1016/j.ultrasmedbio.2015.03.009.
[32] L. Yang, W. Ling, D. He, C. Lu, L. Ma, L. Tang, Y. Luo, S. Chen, Shear wave-based sound touch elastography in liver fibrosis assessment for patients with autoimmune liver diseases, Quant. Imaging Med Surg. 11 (2021) 1532–1542, https://doi.org/10.21037/qims-20-521.
[33] D. Cosgrove, F. Piscaglia, J. Bamber, J. Bojunga, J.-M. Correas, O.H. Gilja, a S. Klauser, I. Sporea, F. Calliada, V. Cantisani, M. D'Onofrio, E.E. Drakonaki, M. Fink, M. Friedrich-Rust, J. Fromageau, R.F. Havre, C. Jenssen, R. Ohlinger, a Săftoiu, F. Schaefer, C.F. Dietrich, EFSUMB guidelines and recommendations on the clinical use of ultrasound elastography. Part 2: clinical applications, Ultraschall Med 34 (2013) 238–253, https://doi.org/10.1055/s-0033-1335375.
[34] G. Diot, S. Metz, A. Noske, E. Liapis, B. Schroeder, S.V. Ovsepian, R. Meier, E. Rummeny, V. Ntziachristos, Multispectral Optoacoustic Tomography (MSOT) of human breast cancer, Clin. Cancer Res. (2017), https://doi.org/10.1158/1078-0432.CCR-16-3200.
[35] S.K. Kalva, X.L. Deán-Ben, M. Reiss, D. Razansky, Spiral volumetric optoacoustic tomography for imaging whole-body biodynamics in small animals, Nat. Protoc. 18 (2023) 2124–2142, https://doi.org/10.1038/s41596-023-00834-7.
[36] T.F. Fehm, X.L. Deán-Ben, S.J. Ford, D. Razansky, In vivo whole-body optoacoustic scanner with real-time volumetric imaging capacity, Optica 3 (2016) 1153, https://doi.org/10.1364/OPTICA.3.001153.
[37] J. Yang, G. Zhang, M. Wu, Q. Shang, L. Huang, H. Jiang, Photoacoustic assessment of hemodynamic changes in foot vessels, J. Biophotonics (2019), https://doi.org/10.1002/jbio.201900004.
[38] M. Xu, L.V. Wang, Universal back-projection algorithm for photoacoustic computed tomography, Phys. Rev. E Stat. Nonlin Soft Matter Phys. (2005), https://doi.org/10.1103/PhysRevE.71.016706.
[39] V. Ntziachristos, D. Razansky, Molecular imaging by means of multispectral optoacoustic tomography (MSOT), Chem. Rev. 110 (2010) 2783–2794, https://doi.org/10.1021/cr9002566.
[40] N. Brillant, M. Elmasry, N.C. Burton, J.M. Rodriguez, J.W. Sharkey, S. Fenwick, H. Poptani, N.R. Kitteringham, C.E. Goldring, A. Kipar, B.K. Park, D.J. Antoine, Dynamic and accurate assessment of acetaminophen-induced hepatotoxicity by integrated photoacoustic imaging and mechanistic biomarkers in vivo, Toxicol. Appl. Pharm. (2017), https://doi.org/10.1016/j.taap.2017.07.019.
[41] N. Roehlen, E. Crouchet, T.F. Baumert, Liver fibrosis: mechanistic concepts and therapeutic perspectives, Cells 9 (2020) 875, https://doi.org/10.3390/cells9040875.
[42] C.-Y. Zhang, W.-G. Yuan, P. He, J.-H. Lei, C.-X. Wang, Liver fibrosis and hepatic stellate cells: etiology, pathological hallmarks and therapeutic targets, World J. Gastroenterol. 22 (2016) 10512–10522, https://doi.org/10.3748/wjg.v22.i48.10512.
[43] Y.H. Feng, X.D. Hu, L. Zhai, J.Bin Liu, L.Y. Qiu, Y. Zu, S. Liang, Y. Gui, L.X. Qian, Shear wave elastography results correlate with liver fibrosis histology and liver function reserve, World J. Gastroenterol. 22 (2016) 4338–4344, https://doi.org/10.3748/wjg.v22.i17.4338.
[44] Q. Lu, C. Lu, J. Li, W. Ling, X. Qi, D. He, J. Liu, T. Wen, H. Wu, H. Zhu, Y. Luo, Stiffness value and serum biomarkers in liver fibrosis staging: study in large surgical specimens in patients with chronic hepatitis B, Radiology 280 (2016) 290–299, https://doi.org/10.1148/radiol.2016151229.
[45] W. Bernal, G. Auzinger, A. Dhawan, J. Wendon, Acute liver failure, Lancet 376 (2010) 190–201, https://doi.org/10.1016/S0140-6736(10)60274-7.
[46] X. Wang, L. Huang, Z. Chi, H. Jiang, Integrated thermoacoustic and ultrasound imaging based on the combination of a hollow concave transducer array and a linear transducer array, Phys. Med. Biol. 66 (2021), https://doi.org/10.1088/1361-6560/abfc91.

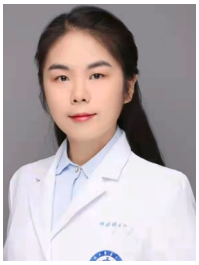

Tingting Qiu is currently a doctor in Department of Ultrasound, West China Hospital, Sichuan University. She received her Ph. D. degree in 2018 from Sichuan University. She completed her post-doctoral fellowship in 2021. Her research mainly focuses on the liver ultrasonography and the clinical application of photoacoustic imaging.

Jinge Yang completed his B.S. and Ph.D. in Electrical Engineering at University of Science and Electronics of China (UESTC) in 2013 and 2019, respectively. His research interests are photoacoustic biomedical imaging techniques and their clinical applications.

Chihan Peng is currently a doctor in Department of Ultrasound, West China Hospital, Sichuan University. He received his Ph.D. degree in 2019 from Sichuan University. He completed his post-doctoral fellowship in 2022. His research mainly focuses on the liver ultrasonography and interventional ultrasound.

Hongjin Xiang is currently a doctoral student in Department of Ultrasound, West China Hospital, Sichuan University. She received her bachelor degree from Sichuan University in 2017. Her research mainly focuses on the liver ultrasonography and the application of thermoacoustic imaging for the liver disease.

Lin Huang is an Associate Professor of School of Electronic Science and Engineering at University of Electronic Science and Technology of China. He received his Ph.D. in 2015 from University of Electronic Science and Technology of China with expertise in thermoacoustic imaging.

Wenwu Ling is an Associate Professor of Department of Ultrasound, West China Hospital, Sichuan University. He graduated from Sichuan University in 2019 with Ph.D. degree. He has been engaged in clinical and scientific research in ultrasound. His research mainly focuses on the contrast-enhanced ultrasound and elastography of abdominal diseases.

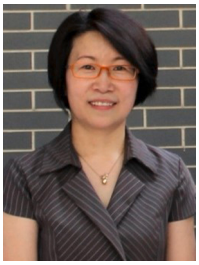

Yan Luo is currently the director and a Professor of Department of Ultrasound, West China Hospital, Sichuan University. She has been engaged in clinical and scientific research in ultrasound. Her current research interests include ultrasonography for abdominal diseases (especially liver diseases) and emerging imaging technologies.